The Astrophysical Journal, 841:101 (15pp), 2017 June 1 https://doi.org/10.3847/1538-4357/aa7263

Quantifying Supernovae-driven Multiphase Galactic Outflows

Miao Li (李邈)[1], Greg L. Bryan[1,2], and Jeremiah P. Ostriker[1]
[1] Department of Astronomy, Columbia University, 550 W. 120th Street, New York, NY 10027, USA; miao@astro.columbia.edu
[2] Simons Center for Computational Astrophysics, 160 5th Avenue, New York, NY 10010, USA
Received 2016 October 27; revised 2017 April 5; accepted 2017 May 8; published 2017 May 31

Abstract

Galactic outflows are observed everywhere in star-forming disk galaxies and are critical for galaxy formation. Supernovae (SNe) play the key role in driving the outflows, but there is no consensus as to how much energy, mass, and metal they can launch out of the disk. We perform 3D, high-resolution hydrodynamic simulations to study SNe-driven outflows from stratified media. Assuming the SN rate scales with gas surface density $\Sigma_{\rm gas}$ as in the Kennicutt–Schmidt relation, we find that the mass loading factor, $\eta_{\rm m}$, defined as the mass outflow flux divided by the star formation surface density, decreases with increasing $\Sigma_{\rm gas}$ as $\eta_{\rm m} \propto \Sigma_{\rm gas}^{-0.61}$. Approximately $\Sigma_{\rm gas} \lesssim 50\,M_{\odot}\,{\rm pc}^{-2}$ marks when $\eta_{\rm m} \gtrsim 1$. About 10%–50% of the energy and 40%–80% of the metals produced by SNe end up in the outflows. The tenuous hot phase ($T > 3 \times 10^5$ K), which fills 60%–80% of the volume at the midplane, carries the majority of the energy and metals in the outflows. We discuss how various physical processes, including the vertical distribution of SNe, photoelectric heating, external gravitational field, and SN rate, affect the loading efficiencies. The relative scale height of gas and SNe is a very important factor in determining the loading efficiencies.

Key words: galaxies: formation – galaxies: ISM – hydrodynamics – ISM: kinematics and dynamics – ISM: structure

1. Introduction

Galactic outflows, widely observed in star-forming galaxies, share a few universal properties. First, outflows are multi-phase. The nearby starburst galaxy M82 is a well-studied example: the outflowing gas consists of a hot phase emitting X-rays, a warm ionized phase probed by Hα, and a cool, dusty phase seen in the infrared. At higher redshifts $z \sim 1$–3, warm/cool outflows have been widely observed in emission and absorption (e.g., Steidel et al. 1996; Shapley et al. 2003; Martin 2005; Weiner et al. 2009; Chen et al. 2010; Genzel et al. 2011; Heckman et al. 2015). Some even contain molecular components (e.g., Walter et al. 2002; Bolatto et al. 2013). Hot winds have also been detected recently (Turner et al. 2015).

Second, the velocities of outflows are several hundred km s^{-1}. This is comparable to the escape velocities from dark matter (DM) halos, indicating that outflows strongly impact galactic evolution, the circumgalactic medium (CGM) and even the intergalactic medium (IGM).

Third, the mass loading factor, defined as the ratio between the outgoing mass flux and the star formation rate (SFR), ranges from 0.01 to 10 (see the review by Veilleux et al. 2005, and references therein). For starburst systems, warm/cool outflows have commonly been reported to have mass loading $\gtrsim$1. But note that large uncertainties in this quantity remain, since the geometry, metallicity, and ionization fraction of the outflows are hard to constrain, and a smaller loading factor ($\sim$10%) is possible (Chisholm et al. 2016).

Galactic outflows play a critical role in galaxy formation. Without them, galaxies in cosmological simulations become too massive, too small, and too metal-enriched (e.g., Scannapieco et al. 2008). Outflows remove gas from galaxies and delay gas infall, thus limiting a galaxy's mass (e.g., Springel & Hernquist 2003). Some ejected mass may eventually fall back at the edge of the galaxy, building the disk from the inside out (Governato et al. 2007; Genel et al. 2015). Outflows also funnel metals from galaxies to their surroundings (e.g., Mac Low & Ferrara 1999; Fujita et al. 2004; Oppenheimer & Davé 2006). This naturally explains why galaxies retain fewer metals than they have produced (Tremonti et al. 2004; Erb et al. 2006), while the CGM and IGM are metal-enriched (Mitchell et al. 1976; Songaila & Cowie 1996; Schaye et al. 2003).

Supernovae (SNe) explosions, the most energetic processes associated with stellar feedback, are thought to be the main driving force of the outflows for galaxies with $M \lesssim 10^{10}\,M_{\odot}$ (Efstathiou 2000). The general picture is that supernova remnants (SNRs) overlap and create hot bubbles, which break out of the disk and launch outflows (Cox & Smith 1974; McKee & Ostriker 1977; Cox 2005). But under what conditions can SNRs overlap? How much energy, mass, and metals are carried in the outflows? Can the outflows escape the galaxy? The answers are essential not only for understanding the observations, but also for building a physically based model of feedback for cosmological simulations and semi-analytic models of galaxy formation. Ad hoc feedback models have been widely used in those works, thus the predictive power is severely limited (see recent reviews by Somerville & Davé 2015 and Naab & Ostriker 2016).

High-resolution numerical simulations are essential to study SN feedback, given the complexities of the multiphase interstellar medium (ISM) and the nonlinear interactions of blast waves. Li et al. (2015) present a high-resolution study to show how SNe shape a patch of the ISM under various conditions. They find, for a given mean gas density, the critical SN rate for hot bubbles to overlap, and to produce a multiphase medium. Various papers have explored how SNe drive outflows from a stratified medium (e.g., de Avillez 2000; Joung & Mac Low 2006; Joung et al. 2009; Hill et al. 2012; Gent et al. 2013; Walch et al. 2015). The solar neighborhood is the most well-studied case, in which a mass loading factor of order unity is found. Creasey et al. (2013) explored a wide parameter space of gas surface density and external gravitational field. Assuming the SN rate correlates with the gas density via the empirical star formation law—the Kennicutt–Schmidt (KS) relation—they

Table 1
Model Description

Run	$\Sigma_{\rm gas}$ ($M_\odot$ pc^{-2})	$\rho_{\rm mid}$ (cm^{-3})	$\dot{\Sigma}_{\rm SFR}$[a] ($M_\odot$ kpc^{-2} yr^{-1})	PEH (erg s^{-1})	Σ_* ($M_\odot$)	$h_{\rm SN,cc}$ (pc)	$v_{\Delta\phi}$[b] (km s^{-1})	$T_{\rm min}$[c] (K)	Res[d] (pc)	l_x (pc)	$R_{\rm inj}$ (pc)	$t_{\rm sim}$[e] (Myr)
Σ1-KS	1	0.011	1.26E-4	2.8E-28	0.5	150	52	300	12.5	1200	80.0	300
Σ1-3KS	⋯	⋯	3.78E-4	⋯	⋯	⋯	⋯	⋯	⋯	⋯	⋯	240
Σ1-10KS	⋯	⋯	1.26E-3	⋯	⋯	⋯	⋯	⋯	⋯	⋯	⋯	130
Σ10-KS	10	0.822	6.31E-3	1.4E-26	35	⋯	89	⋯	2.0	350	12.0	160
Σ10-KS-4g	⋯	1.78	⋯	⋯	180	⋯	178	⋯	⋯	⋯	⋯	64
Σ55-KS-h75	55	8.2	0.158	3.5E-25	35	75	117	⋯	0.75	150	4.5	40
Σ55-KS(-h150)	⋯	⋯	⋯	⋯	⋯	150	⋯	⋯	⋯	⋯	⋯	⋯
Σ55-KS-h300	⋯	⋯	⋯	⋯	⋯	300	⋯	⋯	⋯	⋯	⋯	⋯
Σ55-KS-h450	⋯	⋯	⋯	⋯	⋯	450	⋯	⋯	⋯	⋯	⋯	⋯
Σ55-KS-noPEH	⋯	⋯	⋯	0	⋯	150	⋯	⋯	⋯	⋯	⋯	⋯
Σ55-KS-5PEH	⋯	⋯	⋯	1.75E-24	⋯	⋯	⋯	⋯	⋯	⋯	⋯	⋯
Σ55-KS-1e4K	⋯	⋯	⋯	0	⋯	⋯	⋯	10^4	⋯	⋯	⋯	⋯
Σ150-KS	150	26.3	0.708	1.6E-24	⋯	⋯	160	300	0.60	122	3.0	15

Notes.
[a] SN rate is $\dot{\Sigma}_{\rm SFR}/m_0$, where $m_0 = 150\,M_\odot$.
[b] $v_{\Delta\phi}^2 \equiv 2\Delta\phi(z_{\rm max}) = 2\int_{z=0}^{z_{\rm max}} g_{\rm tot}\,dz$.
[c] Temperature cut-off of the cooling curve.
[d] Resolution at $z \leqslant 500$ pc.
[e] Simulation time.

found that the mass loading decreases with increasing gas surface density.

In this paper, we study SNe-driven outflows from a stratified disk, with various gas surface densities and SN rates. We focus on the following questions. (1) How much energy, mass and metals can SNe launch out of the disk, and how do these change along the KS relation? (2) What physical processes affect the energy, mass, and metal loading? We explore the effects of runaway OB stars, photoelectric heating (PEH), gravitational field, enhanced SN rates, etc. While our simulations focus on regions around the disk (±2.5 kpc), we discuss how our results connect to outflows on a galactic scale.

We organize our paper as follows: we describe the numerical set-ups in Section 2, present the results of the fiducial models in Section 3, and discuss the various processes that can affect the loading efficiencies in Section 4. We discuss the implications of our results in Section 5, and summarize in Section 6.

2. Methods

2.1. Simulation Set-ups

The simulations are performed using the Eulerian hydrodynamical code Enzo (Bryan et al. 2014). We set up a rectangular box with z-dimension of 5 kpc ($-2.5 \leqslant z \leqslant 2.5$ kpc). The midplane of the disk is located at $z = 0$. The horizontal cross section, i.e., x–y plane, is a square. The length of the horizontal dimension, l_x, varies with $\Sigma_{\rm gas}$, as listed in Table 1. The idea is that we adopt higher resolutions for larger $\Sigma_{\rm gas}$, while keeping the corresponding l_x smaller to gain computational efficiency (but sufficiently large to include many SNRs). The grid is refined near the midplane, with two refinement levels. Each refinement increases the resolution by a factor of two. The first level is within $|z| \leqslant 1$ kpc, and the second is $|z| \leqslant 0.5$ kpc. The finest resolution for each run is so chosen that the cooling radius of an SNR $R_{\rm cool}$ is resolved by approximately 12 cells for the initial midplane density $\rho_{\rm mid}$. (For the definition of $R_{\rm cool}$, see Equation (1) of Li et al. 2015.) Kim & Ostriker (2015) have shown that resolving $R_{\rm cool}$ by 10 cells is necessary to well-capture the evolution of an SNR in the Sedov–Taylor phase. Once the ISM becomes multiphase, SNe exploding in the dense region could be under-resolved. But, as we discuss in Section 4.6, this is likely a minor issue.

The boundary conditions are periodic for the x- and y-directions, and outflowing for z. We use the finite-volume piece-wise parabolic method (Colella & Woodward 1984) as the hydro-solver. We use the cooling curve as in Rosen & Bregman (1995), for the temperature range of 300–10^9 K. PEH is time-independent and uniform across the box. The rate of PEH scales linearly with the star formation surface density $\dot{\Sigma}_{\rm SFR}$; for the solar neighborhood model Σ10-KS (see below), we adopt a PEH rate of 1.4×10^{-26} erg s^{-1} per H atom (Draine 2011). We explore the variations of the PEH that deviate from the fiducial settings in Section 4.2.

We have four fiducial runs: Σ1-KS, Σ10-KS, Σ55-KS, Σ150-KS. The number after Σ indicates the gas surface density in units of $M_\odot$ pc^{-2}. The SFRs associated with those runs are along the KS relation. Figure 1 shows the ($\Sigma_{\rm gas}$, $\dot{\Sigma}_{\rm SFR}$) adopted in our simulations, indicated by blue triangles. They are plotted on top of Figure 15 of Bigiel et al. (2008), which shows the observed correlations of $\Sigma_{\rm gas}$ and $\dot{\Sigma}_{\rm SFR}$ for nearby galaxies on sub-kpc scales. Table 1 summarizes the setups of the simulations. Σ10-KS is the model for the solar neighborhood. Variations of fiducial runs are described in Section 4. The gravitational field, initial gas distribution and the model of SN feedback are detailed in the next two subsections. For the fiducial run Σ10-KS, we have carried out a resolution convergence check, where we lower the spatial resolution by a factor of 2. The results agree very well, including the ISM

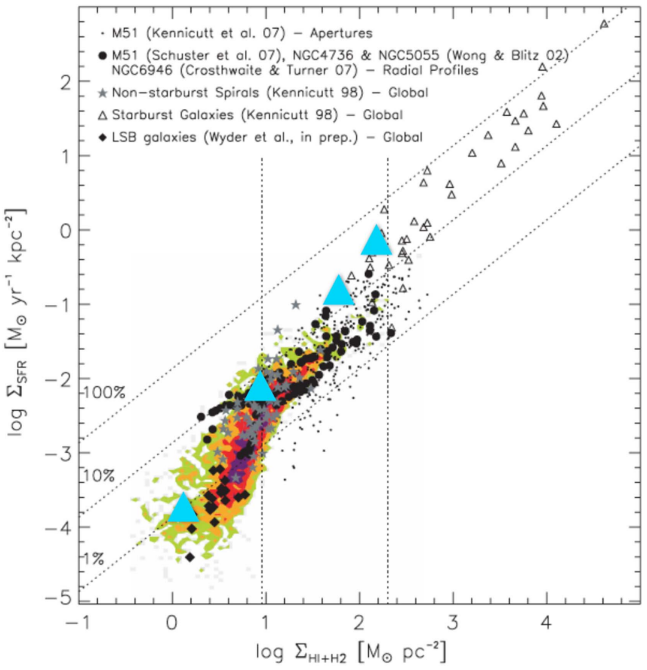

Figure 1. Combinations of $\Sigma_{\rm gas}$ and $\dot{\Sigma}_{\rm SFR}$ adopted in our simulations (blue triangles), plotted on top of Figure 15 of Bigiel et al. (2008), which shows the observed correlations for nearby galaxies at the sub-kpc scale.

properties, volume fraction of difference gas phases, and outflow fluxes.

2.2. Gravitational Fields

The gravitational field ("g-field" hereafter) has two components: a baryonic disk and a DM halo. The disk is modeled as self-gravitating with an iso-thermal velocity dispersion, so its g-field has the form $g = 2\pi G\Sigma_*\tanh(z/z_*)$, where z_* is the scale height of the stellar disk: $z_* \equiv \sigma_*^2/(\pi G\Sigma_*)$, in which σ_* and Σ_* are the velocity dispersion and the surface density of stars, respectively. The height $z_* = 300$ pc is observed for the solar neighborhood (Gilmore & Reid 1983; Binney & Tremaine 2008); we keep it unchanged for all our runs. Since we do not include self-gravity of the gas, we multiply the stellar gravitational field by a factor of $1/f_*$, where $f_* = \Sigma_*/(\Sigma_* + \Sigma_{\rm gas})$. The g-field from the baryonic disk is

$$g_{\rm disk}(z) = \frac{1}{f_*}2\pi G\Sigma_*\tanh\left(\frac{z}{z_*}\right), \quad (1)$$

The g-field from the DM halo is modeled as an NFW profile projected to the z-direction,

$$g_{\rm DM}(z) = \frac{GM_{\rm DM}(r)\,z}{r^3}, \quad (2)$$

where $M_{\rm DM}(r)$ is the enclosed mass of an NFW halo within radius r, so $M_{\rm DM}(r) = 4\pi\rho_{\rm DM}R_s^3\{\ln(1 + r/R_s) - r/(r + R_s)\}$, $R_s = R_{\rm vir}/c$, $\rho_{\rm DM} = 200\,\bar{\rho}_{\rm DM}\,c(1 + c)^2$; $\bar{\rho}_{\rm DM}$ is the mean cosmic DM density at redshift 0, and c is the concentration parameter. For the Milky Way (MW) case, we take $R_{\rm vir} = 200$ kpc, and $c = 12$ (Navarro et al. 1997). Note that r and z are related through $r^2 = z^2 + R_d^2$, in which R_d is the distance from the location of the ISM patch we simulate to the galactic center. The total gravitational field is therefore

$$g_{\rm tot} = g_{\rm disk} + g_{\rm DM}. \quad (3)$$

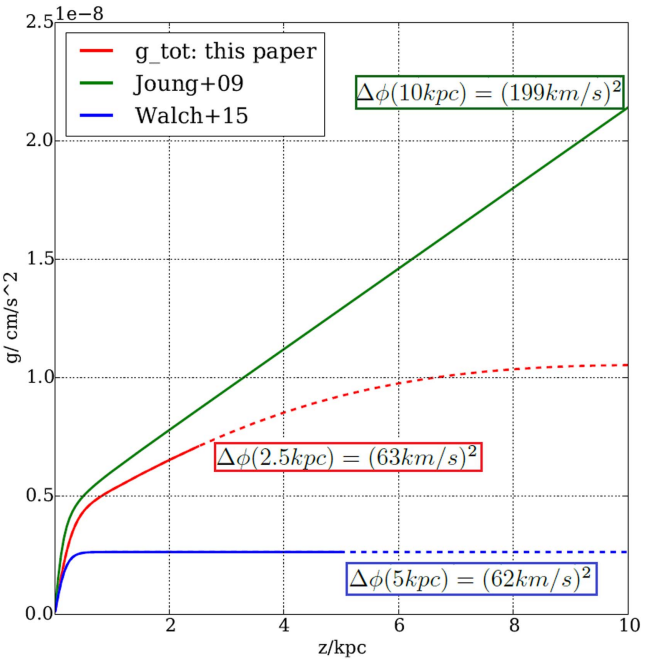

Figure 2. Comparison of g-fields adopted in the literature and this work for the solar neighborhood. The solid lines end at $z_{\rm max}$ of each simulation box, which are 2.5, 5, and 10 kpc for this work, Walch et al. (2015), and Joung et al. (2009), respectively. $\Delta\phi$ for each curve shows the gravitational potential $\Delta\phi(z_{\rm max}) = \int_{z=0}^{z_{\rm max}} g_{\rm tot}dz$. See Section 2.2 for details.

Table 1 lists Σ_* for all of our runs. We keep $R_d = 8$ kpc for all simulations, except for Σ10-KS-4g which has $R_d = 3$ kpc (see Section 4.3 for details). In Table 1 we also include $v_\Delta\phi$ (see the table footnote for its definition) as an indicator for the total potential well for each simulation box.

Note that in the literature the adopted g-field can vary by a factor of a few even when the same "solar neighborhood" is claimed. In Figure 2 we compare our value to a few others. Walch et al. (2015) do not include the DM halo potential, so they have a smaller g; at $z = 5$ kpc, their g-field is about 1/3 of our value. Joung et al. (2009) uses the observed g-field in the solar neighborhood from Kuijken & Gilmore (1989), and extrapolates it into the halo. This works for $z \lesssim$ 1–2 kpc, but above that a simple extrapolation is likely too large. $\Delta\phi$ for each curve shows the gravitational potential $\Delta\phi(z_{\rm max}) = \int_{z=0}^{z_{\rm max}} g_{\rm tot}dz$. The numerical values of $\Delta\phi$ are not negligible compared to the kinetic energies of the outflows, which are typically 100–500 km s^{-1} (see Section 3.2). Consequently, the gravitational field is dynamically important. Indeed, the value of g-field turns out to be important for the loading efficiencies of the outflows (Section 3.3). Any meaningful comparisons between different works should take into account the difference in g-fields.

Initially the gas has a uniform temperature $T_0 = 10^4$ K. We set up the gas initial density to be in hydrostatic equilibrium in the g-field $g_{\rm disk}(z)$, i.e.,

$$\rho = \rho_{\rm mid}\left\{\mathrm{sech}\left(\frac{z}{z_*}\right)\right\}^{2\alpha}, \quad (4)$$

where $\alpha = \gamma\sigma_*^2/(f_* c_{s,0}^2)$, $\gamma = 5/3$ is the adiabatic index of the gas and $c_{s,0}$ is the sound speed for T_0. The power-law decay at large z can result in very low density, so we set up a density floor of $3 \times 10^{-28}\,\mathrm{g\,cm^{-3}}$. Due to the density floor and an extra gravitational field from the DM, the gas is not in perfect hydrostatic equilibrium, but in practice this has little consequence, since the outflowing gas will soon dominate the space above the midplane.

2.3. SN Feedback Models

The SN surface density is related to $\dot{\Sigma}_{\rm SFR}$ by assuming one SN explosion per $m_0 = 150\,M_\odot$ star formation. There are some uncertainties associated with m_0; different works have adopted $m_0 = 100$–$200\,M_\odot$. The distribution of SNe over time is uniform. SNe are randomly located horizontally; in the z-direction, the distribution is stratified. We distinguish two components of SNe: Type Ia and core-collapse SNe. Type Ia constitutes 10% of SN occurrence and core-collapse the rest. Type Ia SNe have an exponential distribution in the z-direction, with a scale height of 325 pc, similar to the old stellar disk (Freeman 1987). Core-collapse SNe have a Gaussian distribution vertically with a scale height $h_{\rm SN,cc} = 150$ pc. We note that, due to runaway OB stars, core-collapse SNe may explode outside of the dense gas layer. We test the sensitivity of the results on $h_{\rm SN,cc}$, as described in Section 4.1.

Each SN is implemented as injecting $E_{\rm SN} = 10^{51}$ erg energy, $m_{\rm SN} = 10\,M_\odot$ mass, and $m_{0,\rm met}$ metals (metals are modeled as "color tracers" that passively follow the mass flux, in arbitrary units), evenly distributed in a sphere. The energy added is 100% thermal. The injection radius $R_{\rm inj}$ varies for $\Sigma_{\rm gas}$, and is chosen to be 0.45–0.50 of the cooling radius for the initial midplane density $\rho_{\rm mid}$. Kim & Ostriker (2015) argued that $R_{\rm inj}/R_{\rm cool} \leqslant 1/3$ is the robust criterion to capture the evolution of an SNR in the Sedov–Taylor phase. Our choice is slightly larger than that.

3. Results of Fiducial Runs

Impacted by SN explosions, the stratified medium quickly becomes multiphase, in which the hot gas occupies a significant fraction of the volume while most mass is in cooler clouds. Cool gas settles down to near the midplane, while outflows are launched. In this section, we first examine the multiphase structure of the ISM, with emphasis on the comparison between our solar neighborhood run with the observations. Then we discuss the velocities of the outflows, and show that the hot phase has the strongest potential to travel to large radii in the DM halo and impact the CGM. Finally we show the mass, energy, and metal loading factors as functions of $\Sigma_{\rm gas}$.

3.1. Multiphase ISM and Outflows

Figure 3 shows slices of the four fiducial runs in the x–z plane. Note that the physical scales of the slices are different from each other. The horizontal lengths are same as the simulation boxes; the vertical dimensions are shown partially. The actual dimensions each slice represents are indicated at the bottom of the temperature slices.

Most of the dense gas stays near the midplane. The medium has multiple phases—a cold phase at a few hundred K, a warm phase at around 10^4 K, and a hot phase at $T \gtrsim 10^6$ K. At the

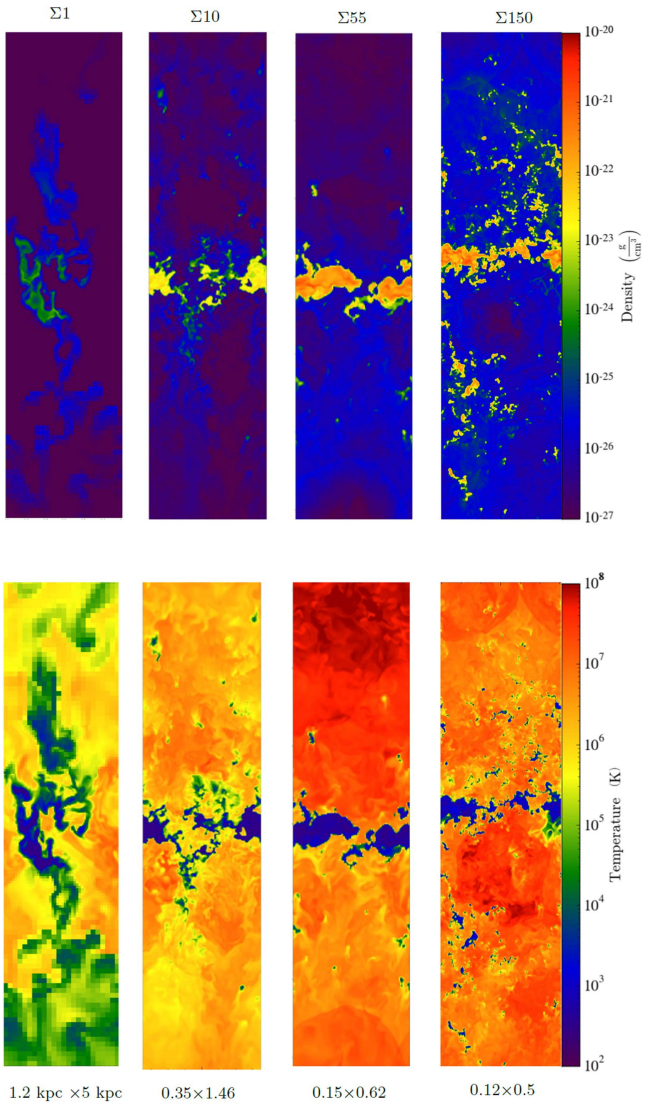

Figure 3. Density and temperature slices of the x–z plane for the four fiducial runs. Note that the physical scales of the slices are different. The dimensions are shown at the bottom of the temperature slices, in the format of "horizontal scale × vertical," in units of kpc.

boundary between the hot and warm/cold phase, gas with intermediate temperature, $10^{5\text{–}6}$ K, is also seen. For all four runs, the hot gas volume fraction is about 60%–80% for the midplane. Hot gas occupies more volume in the halo for higher $\Sigma_{\rm gas}$. Multiphase outflows are being launched from the midplane for all four runs. Cool clouds in the halo are clearly being stripped by the hot, faster gas. The hot phase appears hotter for higher $\Sigma_{\rm gas}$. These qualitative results agree with previous works (McKee & Ostriker 1977; Joung et al. 2009; Creasey et al. 2013).

Figure 4 shows the phase diagram for the run Σ10-KS at $t = 100$ Myr. The color coding indicates the fractional mass in each (density, pressure) bin. The three phases, hot, warm, and cold, are clearly seen. Each of the three phases has some spread in the density distribution. But the majority of them are in pressure equilibrium, with $P/k_{\rm B} \sim 5 \times 10^3$ cm^{-3} K. This is in good agreement with the observations near the solar neighborhood

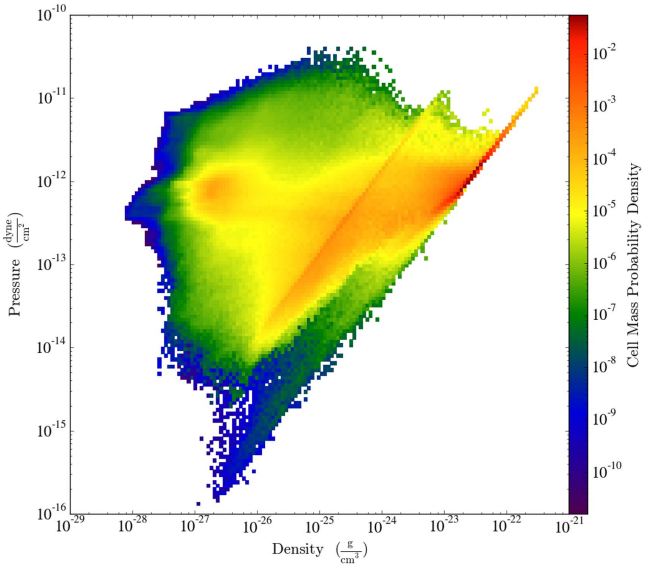

Figure 4. Phase diagram of the gas in Σ10-KS (solar neighborhood model). The color coding shows the fractional mass in each (density, pressure) bin.

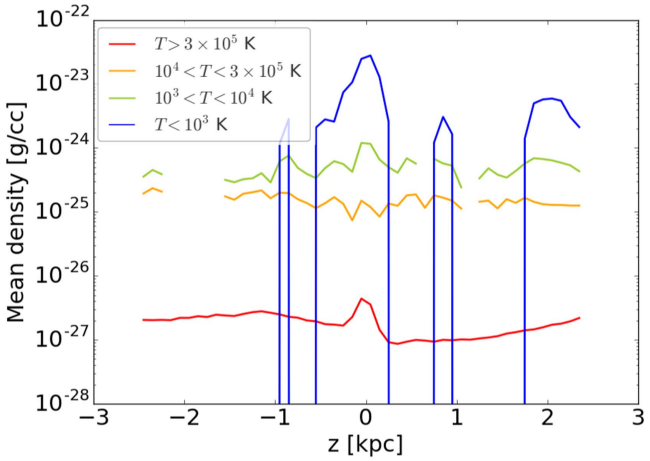

Figure 5. Gas density (volume-weighted) for different phases as a function of z for Σ10-KS at t = 160 Myr.

(Cox 2005). Some mass, which lies in between the two diagonal lines that indicate the standard "warm" and "cold" phases, is out of thermal equilibrium (Heiles & Troland 2003).

Figure 5 shows the density, weighted by volume, of different phases. Hotter phases have progressively smaller densities. The gas density for each phase near the plane is higher than that in the outflows. The warm-hot phase with $10^4 < T < 3 \times 10^5$ K has a slightly lower density than the warm phase. As shown in Figure 3, the warm-hot phase is mostly at the interface between warm clouds and hot gas. Even the coldest phase is seen at large z, even though the volume fraction can be very small. The densities for each phase agree with the observations of the local ISM (see, e.g., Draine 2011)

3.2. Velocity Structure

The velocity structure of the gas determines how far the gas can travel in a gravitational potential. Moreover, the velocity distribution can be observed from the profiles of emission/absorption lines. Since different gas phases have drastically

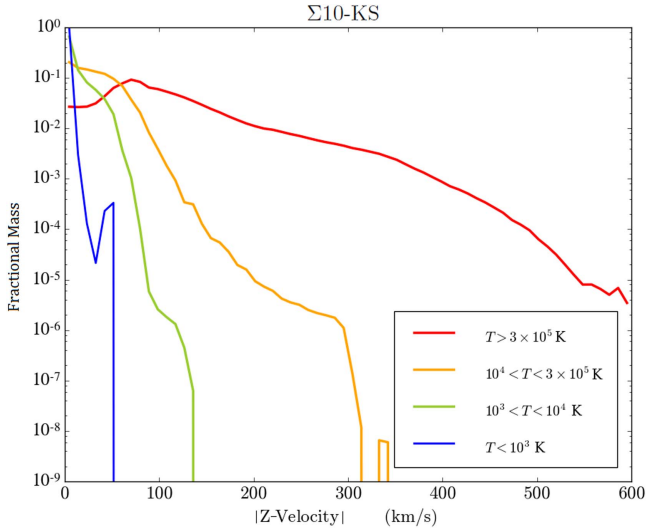

Figure 6. Fractional mass for gas with different z-velocity (absolute value), for the model Σ10-KS at $t = 160$ Myr. Different curves correspond to gas in different temperature ranges. Each curve is normalized to unity.

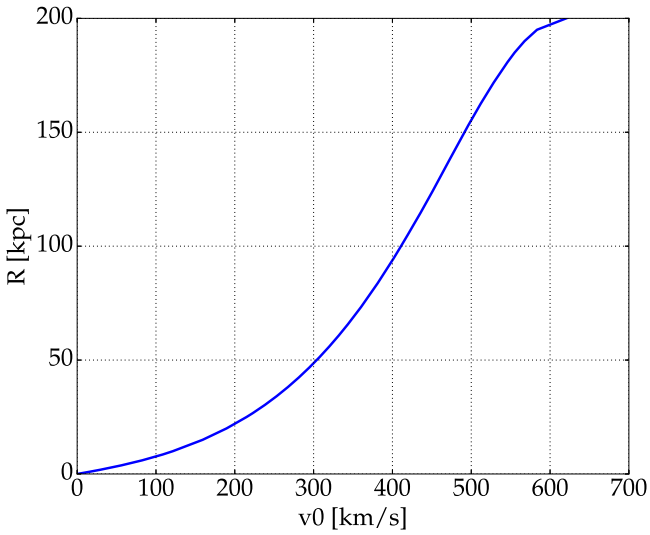

Figure 7. Radius R that a parcel of gas with velocity v_0 can reach from the center of the MW. See Section 3.2 for model details.

different velocities, and observationally they are detected through different line tracers, we hereby show the velocity distribution for each gas phase separately.

Figure 6 shows the z-velocity distribution for the run Σ10-KS at $t = 160$ Myr. The y-axis indicates the fractional mass in each velocity bin. Each curve is normalized to unity. Hotter phases have larger velocities, agreeing with the general observational trend (e.g., Heckman et al. 2001; Rupke et al. 2002), and other simulation works (Creasey et al. 2013; Girichidis et al. 2016b). The hottest phase has the broadest range of velocities, up to $\gtrsim$600 km s^{-1}. A fraction of the warm phase can reach >100 km s^{-1}. The velocities of the cold phase remain small at $\lesssim$50 km s^{-1}.

Our simulations only capture the gas evolution that is relatively close to the midplane, i.e., $|z| \leqslant 2.5$ kpc. One way to relate the "local" outflows to their large-scale evolution is to estimate how far the gas can travel in a given potential. First, let us consider a ballistic evolution. For a parcel of gas with a

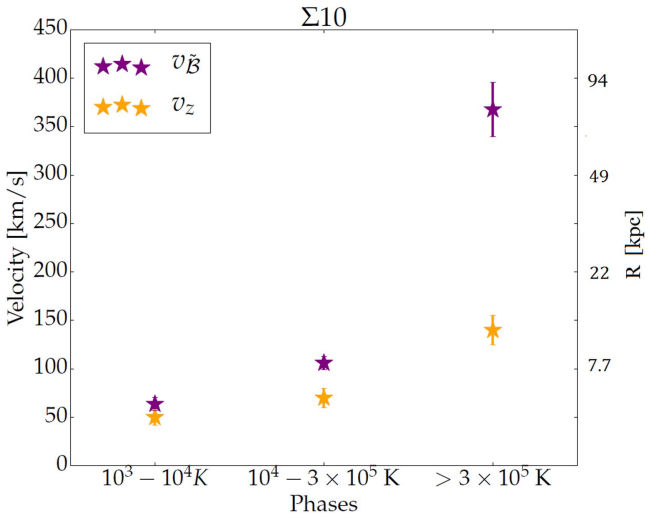

Figure 8. Mass-weighted v_z and $v_{\widetilde{\mathcal{B}}}$ of the outflows in different temperature ranges. *Y*-ticks on the right show *R* corresponding to the velocities on the left, as in Figure 7. See Section 3.2 for details.

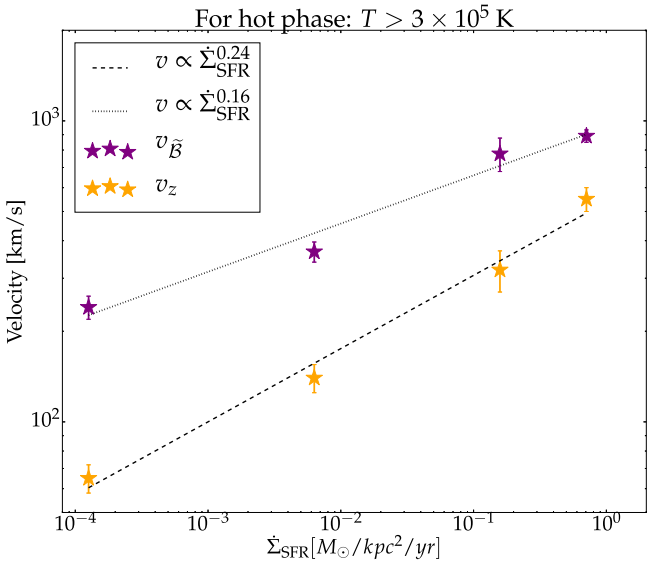

Figure 9. Mass-weighted v_z and $v_{\widetilde{\mathcal{B}}}$ for hot outflows ($T > 3\times10^5$ K), as a function of $\dot{\Sigma}_{SFR}$, for the four fiducial runs. The power-law fits of the data are indicated in the box.

velocity v_0 at the bottom of a potential well, the furthest distance it can reach, *R*, is simply determined by $1/2\ v_0^2 = \Delta\phi(R)$. We use the function $R(v_0)$ to describe such a relation. Figure 7 shows $R(v_0)$ for the MW, for a single stream line that is perpendicular to the disk and goes through the center of the disk. The potential of the DM halo is the same as described in Section 2, and the disk is modeled as a 2D razor-thin disk with a mass $M_D = 5\times10^5\,M_\odot$ and a radius of $R_D = 9.5$ kpc. The mass distribution within the disk is uniform. Thus, along the stream line mentioned above, the *g*-field from the disk has a simple analytic form: $g_D = 2GM_D(1 - z/\sqrt{z^2 + R_D^2})/R_D^2$. From Figure 7, gas with $v_0 \gtrsim 620$ km s^{-1} can escape from the DM halo; gas with $v_0 = 300$ km s^{-1} can travel to $R \sim 50$ kpc, and so on.

We now discuss what should be used as v_0. The naive answer, i.e., the bulk velocity projected to the direction of *g*, may only give a lower bound. For a compressible fluid, it is likely that the gas motion is not ballistic, but thermal energy can later convert to bulk motions. According to the Bernoulli principle, the Bernoulli constant $\mathcal{B} \equiv v_z^2/2 + \gamma/(\gamma-1)P/\rho + \phi$, remains unchanged along a stream line in a steady-state flow (for constant γ). We thus define a modified "Bernoulli velocity" $v_{\widetilde{\mathcal{B}}} \equiv \sqrt{2}\widetilde{\mathcal{B}}^{1/2}$, where $\widetilde{\mathcal{B}} \equiv \mathcal{B} - \phi$. So for a parcel of gas with a bulk velocity v_z and a Bernoulli velocity $v_{\widetilde{\mathcal{B}}}$, the approximate range of radii it can reach is roughly $R(v_0 = v_z) \sim R(v_0 = v_{\widetilde{\mathcal{B}}})$. Note we only aim at a very rough estimate, ignoring cooling, interaction among different gas phases, etc., and assuming $\gamma = 5/3$.

Figure 8 shows the mass-wighted v_z and $v_{\widetilde{\mathcal{B}}}$ for different phases for the fiducial run Σ10-KS. The *y*-axis on the right shows *R* corresponding to the velocities on the left axis. Only gas at $|z| \geqslant 1$ kpc is included. The data are averaged over the last 20% of the simulation time. The error bars indicate time variations. The hot gas is affected more by each SN explosion, thus its properties vary stronger with time. Both v_z and $v_{\widetilde{\mathcal{B}}}$ increase with gas temperature. The hottest phase, given its large v_z (∼150 km s^{-1}) and $v_{\widetilde{\mathcal{B}}}$ (∼370 km s^{-1}), would travel much further into the halo, to about 30–70 kpc. Since the majority of the hot gas would not escape from the DM halo, large-scale fountain flows would form. The small velocities of the cool phase imply that they would fall back at below 10 kpc, unless being accelerated significantly. The velocity of the warm-hot phase, with $T = 10^4$–3×10^5K, is much closer to the warm phase than the hot. The ratio $v_{\widetilde{\mathcal{B}}}/v_z$ is largest for the hot phase, meaning that a significant fraction of the energy is thermal, which may convert to the bulk motion at large radii. For cooler phases, in contrast, most energy is kinetic. Note that the fiducial run is for the solar neighborhood, and is not representative of the MW disk in general. We discuss the model for the MW-average, Σ10-KS-4g, in Section 4.3. Hot flows are much faster there than the solar neighborhood, and can thus have a much broader impact on the CGM (see Section 4.3 for details).

Figure 9 shows the mass-weighted v_z and $v_{\widetilde{\mathcal{B}}}$ for the hot outflows, as a function of $\dot{\Sigma}_{SFR}$ for the four fiducial runs. Again, the error bars show time variation. Both v_z and $v_{\widetilde{\mathcal{B}}}$ increase with SFR. The velocities for the Σ1-KS run are 60–200 km s^{-1}, and rise to 600–900 km s^{-1} for Σ150-KS. The large velocities imply that the hot outflows can travel far, and even escape from the halo potential. This suggests that hot outflows play a critical role in regulating the CGM and even the IGM.

We find that $v_z \propto \dot{\Sigma}_{SFR}^{0.24}$, and $v_{\widetilde{\mathcal{B}}} \propto \dot{\Sigma}_{SFR}^{0.16}$. Observationally, while there is little direct constraint on velocities for hot gas, for the warm/cool phases, Martin (2005) and Weiner et al. (2009) found $v \propto \mathrm{SFR}^{0.3-0.35}$ for galactic-scale outflows. Our findings seem to indicate that the velocity dependence on SFR for the hot gas is weaker than for the cooler phases.

3.3. Loading Factors

In this section, we discuss the loading capability of the outflows. We define outflows to be at $|z| \geqslant 1$ kpc and with outgoing *z*-velocity. We find in our simulations that the outflow fluxes show little variation with *z* at $|z| \geqslant 1$ kpc.

The mass loading factor η_m is defined as the ratio between the outflowing mass flux and $\dot{\Sigma}_{SFR}$, that is,

$$\eta_m \equiv \frac{\langle \rho v_z \rangle}{\dot{\Sigma}_{SFR}}. \quad (5)$$

The outflow flux includes both sides of the plane, and "⟨...⟩" denotes averaging over space ($1 \leqslant |z| \leqslant 2.5$ kpc) and time (last 40% of $t_{\rm sim}$).

The energy loading factor $\eta_{\rm E}$ is the ratio between the z-component of the energy flux and the energy production rate by SNe, that is,

$$\eta_{\rm E} \equiv \frac{\langle (e_{\rm k} + e_{\rm th}) v_z \rangle}{\dot{\Sigma}_{\rm SFR} E_{\rm SN}/m_0}, \quad (6)$$

where $e_{\rm k}$ and $e_{\rm th}$ are the kinetic and thermal energy per unit volume.

The metal loading factor $\eta_{\rm met}$ is the ratio of the z-component of the metal flux to the metal production rate by SNe:

$$\eta_{\rm met} \equiv \frac{\langle \rho_{\rm met} v_z \rangle}{\dot{\Sigma}_{\rm SFR}\, m_{0,\rm met}/m_0}, \quad (7)$$

where $\rho_{\rm met}$ is the density of metals, and $m_{0,\rm met}$ is the mass of metals each SN produces (in arbitrary units, see Section 2.3). Note that we assume the metals are solely produced by SNe, and the ISM is otherwise pristine.

Figure 10 summarizes the loading factors and the volume fraction of each gas phase in the outflows as functions of $\Sigma_{\rm gas}$, for the four fiducial runs. For the loading factors we show the total loading, which includes all gas phases, as well as that of the hot outflows only. The error bars indicate the standard deviation of the time variation.

We find that $\eta_{\rm m}$ decreases monotonically with increasing $\Sigma_{\rm gas}$. The largest mass loading is about 6 for Σ1-KS. For the solar neighborhood case, i.e., Σ10-KS, our $\eta_{\rm m}$ is around 2–3. For our highest density case Σ150-KS, $\eta_{\rm m}$ is only 0.2. The fraction of the mass loading contributed from the hot gas is about 1/3, except for Σ150-KS, where most of the mass flux is hot. The warm phase dominates the outflowing mass flux except when $\dot{\Sigma}_{\rm SFR}$ is very high.

We fit our mass loading factor by a simple power-law function of $\Sigma_{\rm gas}$:

$$\eta_{\rm m} = 7.4\left(\frac{\Sigma_{\rm gas}}{1\, M_\odot\ {\rm pc}^{-2}}\right)^{\alpha_{\rm ml}},\ \alpha_{\rm ml} = -0.61 \pm 0.03. \quad (8)$$

For the hot gas, the mass loading factor is

$$\eta_{\rm m,h} = 2.1\left(\frac{\Sigma_{\rm gas}}{1\, M_\odot\ {\rm pc}^{-2}}\right)^{\alpha_{\rm ml,h}},\ \alpha_{\rm ml,h} = -0.61 \pm 0.03. \quad (9)$$

Creasey et al. (2013) have found a sharper decline, with $\alpha \approx -1.1$. Our results agree with theirs for $\Sigma_{\rm gas} \lesssim 10\, M_\odot\ {\rm pc}^{-2}$, but there are relatively large discrepancies at higher densities; see Section 4.5 for a discussion. The X-ray emission from the halo of edge-on galaxies suggests a decreasing mass loading of hot gas for higher SFR (Zhang et al. 2014; Bustard et al. 2016; Wang et al. 2016), consistent with our results.

The energy loading factor $\eta_{\rm E}$ shows surprisingly little dependence on $\Sigma_{\rm gas}$. Despite a factor of 150 span of $\Sigma_{\rm gas}$, $\eta_{\rm E}$ stays at about 10%–30%. This means a significant fraction of SN energy goes into the outflows. There is no obvious trend of $\eta_{\rm E}$ as a function of $\Sigma_{\rm gas}$. The hot gas contains the majority, >90%, of the outflow energy.

The metal loading factor $\eta_{\rm met}$ shows somewhat larger variation than $\eta_{\rm E}$, although again we do not find an apparent dependence on $\Sigma_{\rm gas}$. Overall, a quite large fraction of metals goes into the outflows, about 40%–90%. Hot outflows carry 35%–60% of the metals produced by SNe. While the warm/cool phase may fall back to the disk later, the hot gas has the potential to travel much further, even to escape the halo (see Section 3.2), and metals will be carried along. The mass–metallicity relation of galaxies implies that a significant fraction of all metals ever produced are no longer in galaxies (Tremonti et al. 2004; Erb et al. 2006). Our numbers agree with this general picture.

The volume in outflows is progressively occupied by the hot gas as $\Sigma_{\rm gas}$ becomes larger. The cold phase with $T < 10^3$ K has a negligible volume fraction, thus we omit it in the plot. For Σ1-KS, the volume is equally shared by the warm and hot phases; for Σ55-KS, more than 90% of volume is hot; for Σ150-KS, the outflows are completely dominated by the hot phase.

4. Effects of Several Physical Processes

4.1. SNe Scale Height

Where SNe explode is critical for feedback efficiency. An SN exploding in a dense medium quickly radiates away its energy, and has little impact on the large-scale ISM, let alone contributing to driving winds (Girichidis et al. 2016b). On the other hand, if an SN explodes in an environment dominated by tenuous gas, then the cooling is much less efficient, and a significant fraction of energy can be preserved (e.g., Hennebelle & Iffrig 2014; Simpson et al. 2014; Gatto et al. 2015; Li et al. 2015; Walch et al. 2015). One key factor to determine where SNe explode is the fact that a significant fraction of OB stars are "runaways," that is, they have high velocities. A simple calculation shows that OB runaways can migrate a few tens to a few hundreds of parsecs before exploding as SNe (Li et al. 2015). This greatly facilitates SN feedback by allowing some of them to release their energy outside the dense SF regions.

In principle, the locations of core-collapse SNe depend on the velocities of OB stars, their lifetimes, the external gravitational field, close encounters with other stars, etc. One can also infer the SNe explosion sites from the spatial distribution and the velocities of pulsars (Narayan & Ostriker 1990). In this paper, we do not aim to model the location of SNe from first principles, but simply explore how sensitively the outflow properties depend on the vertical distribution of SNe. For the fiducial runs we have the $h_{\rm SN,cc} = 150$ pc. Now we experiment with $h_{\rm SN,cc}$. We take the run of Σ55-KS and change $h_{\rm SN,cc}$ to 75, 300, and 450 pc. In Table 1, they are identified by the names Σ55-KS-h75, Σ55-KS-h300, and so on.

Figure 11 shows the mass, energy, and metal loading factors for different $h_{\rm SN,cc}$. Interestingly, $\eta_{\rm m}$ depends on $h_{\rm SN,cc}$ in a different way from $\eta_{\rm E}$ and $\eta_{\rm met}$. As $h_{\rm SN,cc}$ increases, $\eta_{\rm m}$ first increases, reaches a peak at $h_{\rm SN,cc} = 150$ pc, and then declines. The loading factors $\eta_{\rm E}$ and $\eta_{\rm met}$ increase monotonically with $h_{\rm SN,cc}$, and reach a plateau at $h_{\rm SN,cc} \gtrsim$ 150–300 pc. For $h_{\rm SN,cc} =$ 75 pc, most SNe are buried in the midplane, and radiate their energy there, so the feedback is least efficient. As $h_{\rm SN,cc}$ becomes larger, more SNe explode in the low-density disk–halo interface, resulting in a more effective energy and metal loading. The non-monotonic dependence on $h_{\rm SN,cc}$ of $\eta_{\rm m}$ can be understood in this way: when $h_{\rm SN,cc}$ is too small, most energy radiates away in the disk, so the energy insufficiency is the limiting factor for the mass loading; when $h_{\rm SN,cc}$ is too large, the outflowing mass is simply

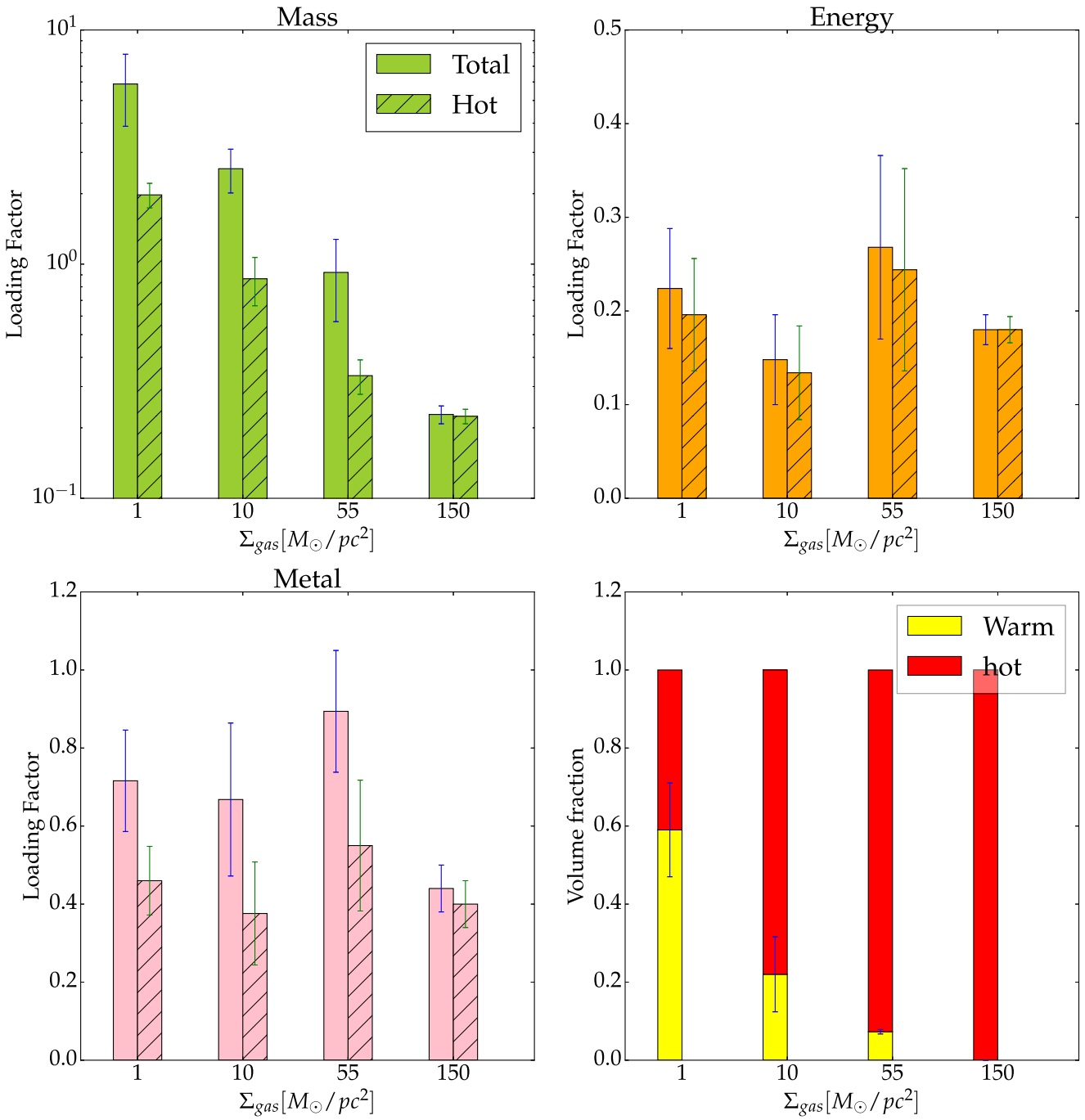

Figure 10. Loading factors and volume fraction of each gas phase as functions of $\Sigma_{\rm gas}$. The quantities are calculated for outflowing gas at $|z| \geqslant 1$ kpc. "Hot" and "warm" here denote $T > 3 \times 10^5$ K, and $10^4 < T < 3 \times 10^5$ K, respectively. See Section 3.3 for details.

SNe ejecta, with little ISM involved. Consequently, the maximum $\eta_{\rm m}$ occurs in between those two extremes. We find that $\eta_{\rm m}$ achieves unity when $h_{\rm SN,cc} = 150$ pc, while $\eta_{\rm m} \lesssim 0.2$ for other cases. For $h_{\rm SN,cc} \gtrsim 300$ pc, 40%–50% of energy and 80% of metals produced by SNe end up in the outflows.

4.2. Photoelectric Heating

In the absence of SN explosions, PEH maintains a two-phase warm/cold ISM (Draine 1978; Wolfire et al. 1995). The value of the PEH rate $\Gamma_{\rm PEH}$ determines the relative amount of mass in the two phases and the pressure of the ISM (Wolfire et al. 2003). With SNe, $\Gamma_{\rm PEH}$ is an important factor in determining whether the ISM is in a thermal runaway state or not (Li et al. 2015). A higher $\Gamma_{\rm PEH}$ keeps more gas in the warm phase and increases the ISM pressure, thus limiting the size of the hot bubbles of SNRs. As a result, SNRs may not effectively overlap, and each SNR loses the majority of its energy at the cooling stage. Therefore little energy is left to drive an outflow. We thus expect that $\Gamma_{\rm PEH}$ is important in determining the outflow properties.

In this section we study the effect of different values of $\Gamma_{\rm PEH}$. We note that $\Gamma_{\rm PEH}$ depends on many factors: the far-UV background, dust abundance, work function of the dust grains,

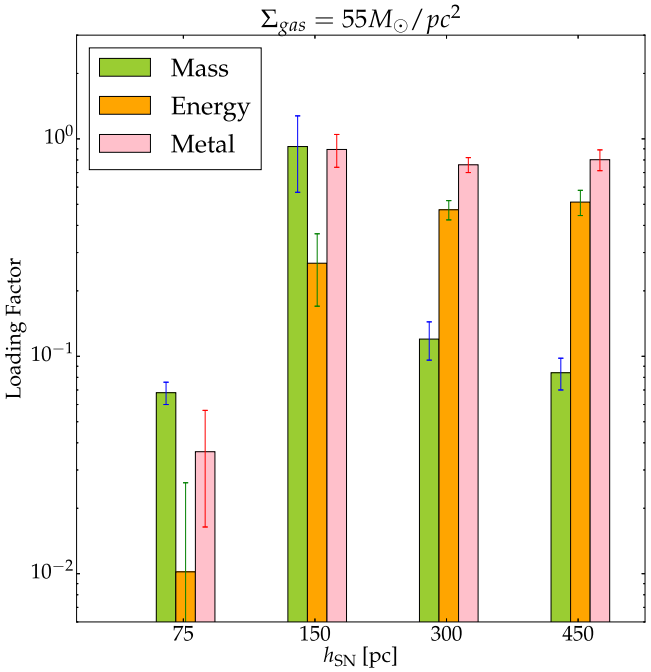

Figure 11. Loading factors for different SN scale heights $h_{\rm SN,cc}$ for the model Σ55-KS. See Section 4.1 for details.

ionization fraction of the gas, etc. (Draine 2011). A star-forming region has a very complex structure with strong and time-varying radiation background with both ionizing and non-ionizing photons. The radiation background also varies in space, and is much more intense around OB stars. The exact condition is thus hard to determine. For simplicity, we keep $\Gamma_{\rm PEH}$ constant in time and uniform in space for each simulation, but just change $\Gamma_{\rm PEH}$ to explore its effect. Note that some previous works adopt a cooling curve with a cut-off at 10^4 K, which prohibits the formation of the cold phase. This is similar to the effect of a very high $\Gamma_{\rm PEH}$. We include a discussion of the cooling curve cut-off as well.

We compare four runs that have $\Sigma_{\rm gas} = 55\,M_\odot\,{\rm pc}^{-2}$. The set-ups are identical (including the SN rate) except $\Gamma_{\rm PEH}$:

(a) $\Gamma_{\rm PEH} = 0$ ("Σ55-KS-noPEH");
(b) $\Gamma_{\rm PEH} = 3.5 \times 10^{-25}$ erg s^{-1} (fiducial, "Σ55-KS");
(c) $\Gamma_{\rm PEH} = 1.75 \times 10^{-24}$ erg s^{-1} ("Σ55-KS-5PEH");
(d) cooling curve has a cut-off at $T_{\rm min} = 10^4$ K ("Σ55-KS-1e4K").

In Figure 12 we show the slices for the fiducial run and Σ55-KS-1e4K. Adopting $T_{\rm min} = 10^4$ K results in a much larger scale height of gas (defined as enclosing 80% of the mass in the box), $h_{\rm gas} \sim 200$ pc, in contrast to $h_{\rm gas} \sim 10$ pc for the fiducial case. Assuming hydrostatic equilibrium, i.e., gravity is balanced by the thermal and turbulence pressure,

$$h_{\rm gas} \sim 140{\rm pc}\left(\frac{1+\mathcal{M}^2}{2}\right)\left(\frac{T_{\rm gas}}{10^4\ {\rm K}}\right)\left(\frac{5\times10^{-9}\ {\rm cm\ s^{-2}}}{g}\right), \quad (10)$$

where $\mathcal{M}$ is the local Mach number of the gas, which is on the order of unity. Note that in our simulations, SNe have a Gaussian distribution with $h_{\rm SN,cc} = 150$ pc. So for the fiducial case, once the multiphase medium is formed, most SNe explode *outside* of the gas layer, whereas for Σ55-KS-1e4K, most SNe explode *within* the gas layer. For the latter, since the

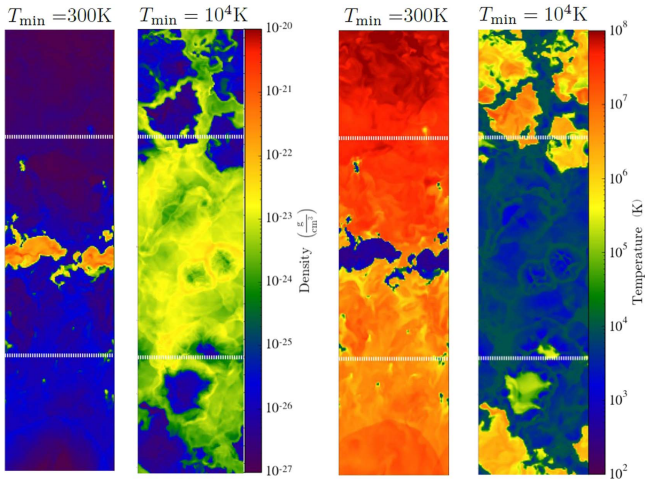

Figure 12. Temperature and density slices of two runs with $\Sigma_{\rm gas} = 55\,M_\odot\,{\rm pc}^{-2}$: left—fiducial (Σ55-KS); right—cooling curve has a cut-off at $T_{\rm min} = 10^4$ K (Σ55-KS-1e4K). The snapshots are taken at $t = 41$ Myr. The slices only include the region at $|z| \leqslant 325$ pc. The white dashed lines indicate the scale height of core-collapse SNe $h_{\rm SN,cc} = 150$ pc. The cut-off of the cooling curve at 10^4 K results in a much larger gas scale height. As a result, most SNe energy is lost through radiative cooling in the dense gas layer.

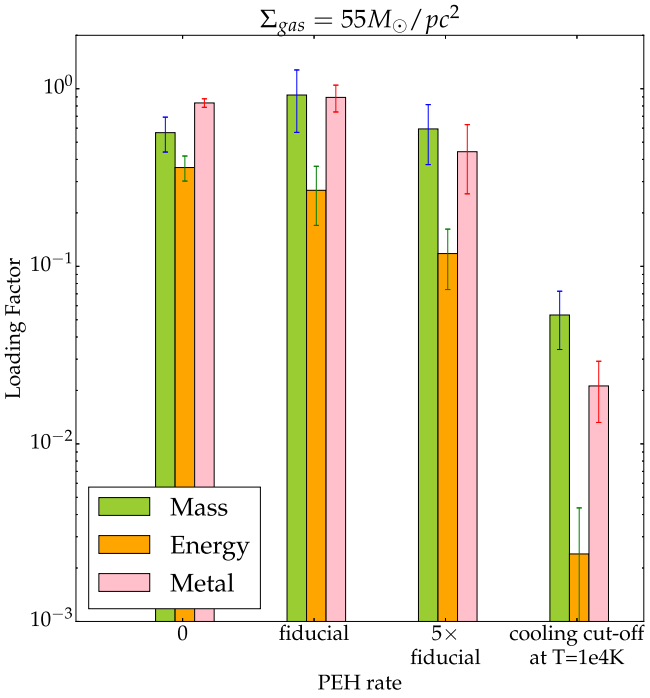

Figure 13. Loading factors for different PEH rates, for the model with $\Sigma_{\rm gas} = 55\,M_\odot\,{\rm pc}^{-2}$. See Section 4.2 for details.

ISM is not in a thermal runaway state, most of the energy released from SNe is radiated away. Therefore, a cooling curve with $T_{\rm min} = 10^4$ K gives much smaller energy, mass, and metal loading. It is true that we are adopting a temperature cut of 300 K, and the actual temperature of the cold phase can be even lower. But our temperature cut is low enough to allow the ISM at midplane to undergo a thermal runaway—as mentioned in Section 3.1, all fiducial runs have a volume fraction of hot gas of 60%–80% at midplane. We thus believe that our results do not suffer from a qualitatively erroneous cooling loss, while a temperature cut at 10^4 K may do so.

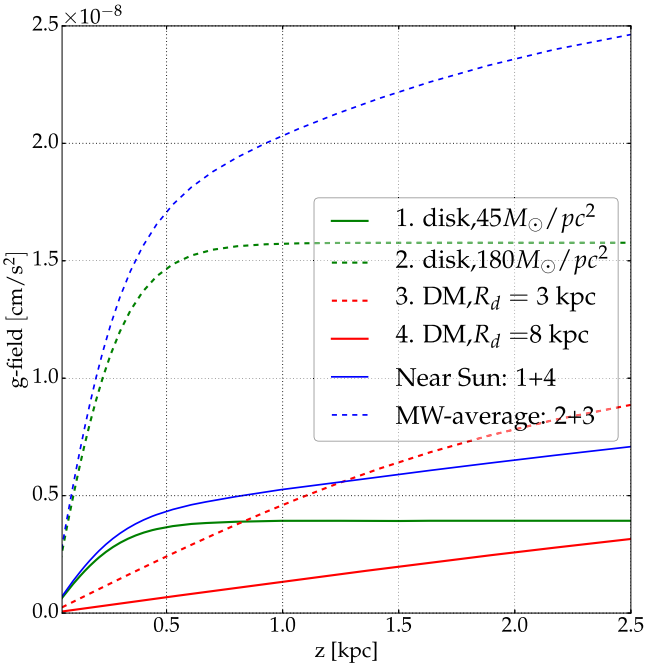

Figure 14. External gravitational fields adopted for the solar neighborhood (Σ10-KS) and the MW-average (Σ10-KS-4g). Different components are shown separately. See Section 4.3 for relevant discussions.

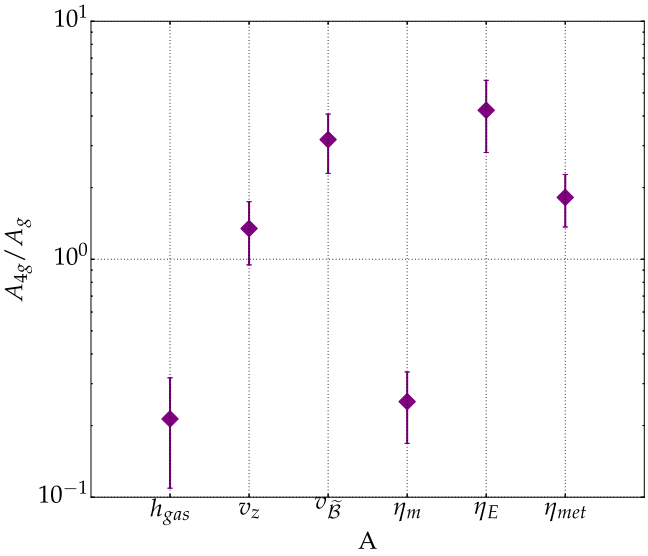

Figure 15. Ratio of properties between two runs with different gravitational fields: Σ10-KS-4g (MW-average) and Σ10-KS (solar neighborhood). See Section 4.3 for a discussion.

Figure 13 compares the loading factors of all four runs in this section. The simulation Σ55-KS-1e4K gives an energy loading two orders of magnitude smaller than the fiducial run; $\eta_{\rm m}$ is smaller by a factor of 10, and $\eta_{\rm met}$ by a factor of 30. This indicates that if the formation of the cold phase is prohibited, the power of SN feedback is severely underestimated. Comparing the three runs with different $\Gamma_{\rm PEH}$, we find that when $\Gamma_{\rm PEH}$ is higher, the energy loading is smaller, as expected, since $h_{\rm gas}$ is increasingly larger for stronger PEH. The mass and metal loadings do not show significant variation. This is likely due to the following two effects counteracting each other: a smaller $\eta_{\rm E}$ means that less energy is available to drive the mass out, while a larger $h_{\rm gas}$ is favorable to loading more gas, as discussed in Section 4.1.

4.3. External Gravitational Field

To explore the effect of external gravitational field on the outflows, we take the MW as an example. The fiducial run Σ10-KS uses the gravitational field in the solar neighborhood, which has $\Sigma_{\rm gas} = 10\,M_\odot\,{\rm pc}^{-2}$, $\Sigma_* = 35\,M_\odot\,{\rm pc}^{-2}$, and a displacement $R_d = 8$ kpc from the center of the DM halo. This g-field is smaller than the inner part of the MW disk. We set up a higher gravity run Σ10-KS-4g, which uses a g-field more typical for the inner MW disk, with $\Sigma_{\rm gas} = 10\,M_\odot\,{\rm pc}^{-2}$, $\Sigma_* = 180\,M_\odot\,{\rm pc}^{-2}$ and $R_d = 3$ kpc. The g-field is approximately four times that of the solar neighborhood. Figure 14 shows the different components of the two g-fields.

Naively, one would think a larger gravity would make the feedback less effective, as gravity drags the outflows toward the disk. While this is generally true for regions away from the launching region, the situation near the disk is more complex. We plot the ratios of the loading factors between Σ10-KS-4g and Σ10-KS in Figure 15. The comparison is done for the time interval $t = 40$–64 Myr, and the error bar shows the standard deviation of time variation. While $\eta_{\rm m}$ is indeed smaller by a factor of 3–4 in the higher gravity case, the energy loading $\eta_{\rm E}$ is, nevertheless, a factor of 3–5 larger. The metal loading $\eta_{\rm met}$ is also larger by a factor of 1.5.

How can we understand this? It turns out that the dominant impact of larger g-field here is to reduce $h_{\rm gas}$. As we also show in Figure 15, a factor of 4 increase in gravity results in roughly the same factor of decrease in $h_{\rm gas}$. This is expected for gas in hydrostatic equilibrium (Equation (10)). Since we keep $h_{\rm SN,cc}$ the same for the two runs, a smaller $h_{\rm gas}$ exposes more SNe in the low-density halo. As discussed in Section 4.1, more SNe above the gas layer can lead to a smaller $\eta_{\rm m}$ but larger $\eta_{\rm E}$ and $\eta_{\rm met}$. Since less mass is heated by more energy, $v_{\widetilde{\mathcal{B}}}$ of the outflowing gas is much larger in Σ10-KS-4g, by a factor of 3 than in the solar neighborhood. The values of v_z and $v_{\widetilde{\mathcal{B}}}$ are about 175 km s^{-1} and 980 km s^{-1}, respectively; the latter is even larger than the escape velocity of the MW halo ∼620 km s^{-1}. Thus the outflows for the MW-average are much more vigorous, which can broadly impact the CGM and even the IGM (see further discussion in Section 5.1).

4.4. Enhanced SNe Rates

For our fiducial runs, we assume that $\dot{\Sigma}_{\rm SFR}$ scales with $\Sigma_{\rm gas}$ as in the KS relation. Although the KS relation is well-established at scales $\gtrsim$kpc, variation appears at smaller scales (Heiderman et al. 2010). In particular, star formation tends to occur in groups, and the OB stars are clustered in space and time. The sizes of our simulation boxes are in the sub-kpc regime, so it will be interesting and relevant to discuss the variation on the SN rate. In this section, we discuss the effect of enhanced SN rates on the outflows. We are interested in how the energy, mass, and metal loading efficiencies depend on the SN rates. Since the interaction of blast waves is highly nonlinear, it is non-trivial to predict whether the impact of multiple SNRs would be a simple add-up, to reinforce, or to cancel each other out.

We take the run Σ1-KS, and increase the SN rate by 3× and 10×. These runs are listed in Table 1 as "Σ1–3KS" and

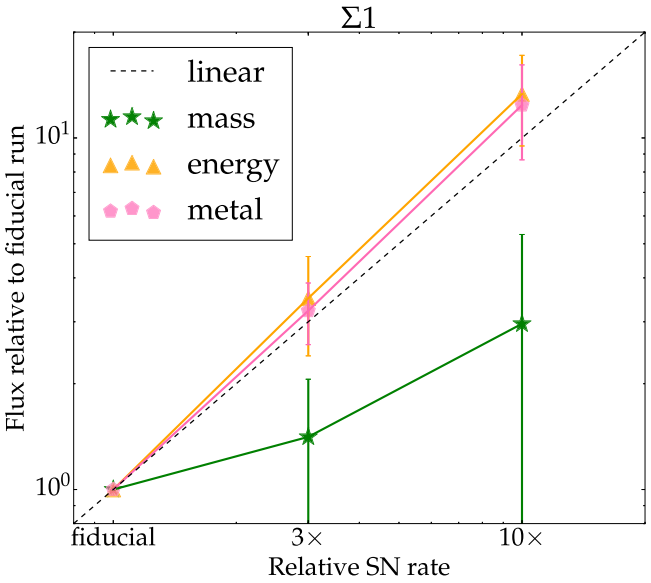

Figure 16. Relative fluxes of mass, energy, and metal as a function of SN rate for $\Sigma_{\rm gas} = 1\,M_\odot\,{\rm pc}^{-2}$. The fiducial run follows the KS relation, while the "enhanced-rate" runs have SN rates increased by 3 and 10 times, respectively. The dashed black line indicates a linear relation. See Section 4.4 for discussions.

"Σ1–10KS." Figure 16 shows the mass, energy, and metal fluxes of the outflows relative to the fiducial run. The mass flux scales with the SN rate in a sub-linear manner. A factor of 3 and 10 increase in the SN rate only results in, on average, a factor of 1.5 and 3 enhancement in the mass flux, respectively. The energy and metal fluxes, on the other hand, show a roughly linear correlation with the SN rate. This means that the mass loading is less efficient when we increase the SN rate, while the energy and metal loading factors remain roughly constant for different SN rates.

We caution that, even for the fiducial run, which has the lowest SN rate, most of the midplane is in a hot-dominated multiphase state. The sub-linear dependence of the mass flux and roughly linear dependence of the energy and metal flux are likely to be the features in this regime. If, for example, one starts with an SN rate sufficiently small so that the SNRs in the disk would not overlap, then the enhancement of the SN rate would lead to a transition from a steady-state ISM to forming outflows. As a result, the dependence of all fluxes on the SN rate would be super-linear. But since we are, in this paper, interested in the regime where outflows are generated, we do not explicitly explore the parameter space that leads to a steady-state ISM. Indeed, for all four fiducial runs, which are along the KS relation, the ISM at the midplane is in a thermal runaway state and outflows are being launched. Therefore, the scaling relations as shown in Figure 16 should hold for other $\Sigma_{\rm gas}$ cases as well.

Girichidis et al. (2016b) find that clustering of some SNe does not affect the mass outflow rate. We find a very mild increase in mass flux, although with large fluctuations. Within error bars our results are consistent with each other. Overall, once the ISM is hot-dominated, clustering of SNe does not help with the loading factors, and may even be negative for loading mass.

4.5. Comparison with Other Works

Girichidis et al. (2016b) have found that for the solar neighborhood, SNe can blow away most of the gas in the midplane, and drive outflows with a mass loading up to 10. This is higher than our value, which is around 2–3. Compared to our model, their SN scale height is smaller, 50 pc, which causes an "explosive" thermal-runaway at the midplane. Initially there is no leak of those hot gases, whose high-pressure propels the neutral gas layer up, like the formation of a super-bubble. Later on, the Rayleigh–Taylor instability will develop, the shell will fragment, and hot gas leaks to form winds (Mac Low & Ferrara 1998). For our case, $h_{\rm SN,cc}$ is larger, meaning that SNe are more spread-out in the z-direction. We do see warm shells of gas being driven out initially, but that does not involve too much mass, and would later either go beyond the box, or fragment and fall back. Our loading factors are calculated after those initial transient stages. Additionally, a weaker g-field (see Section 2.2) may also partially account for their relatively large mass loading.

Creasey et al. (2013) study SNe-driven outflows covering a broad parameter space of $\Sigma_{\rm gas}$ and g-field. The g-field can be expressed using the gas fraction, $f_{\rm g} \equiv \Sigma_{\rm gas}/(\Sigma_{\rm gas} + \Sigma_*)$. We here conduct a one-on-one comparison between our fiducial runs and their models. We note that their boxes are smaller in the vertical direction, $|z| \leqslant 0.5$ kpc, and their outflow fluxes are measured at the outer boundaries; whereas ours are averaged over $1 \leqslant |z| \leqslant 2.5$ kpc. Our fiducial runs that overlap with their models are Σ10-KS, Σ55-KS, and Σ150-KS, which corresponds to $(\Sigma_{\rm gas}, f_{\rm g}) = (10, 0.15)$, (55, 0.5), and (150, 0.7), respectively. We convert our g-field from the DM halo to an equivalent surface density of $\approx 25\,M_\odot\,{\rm pc}^{-2}$. We interpolate their data if there is no direct comparison.

For the solar neighborhood, their mass loading factor is about unity, and energy loading ("thermalization factor" in their terminology) is around 0.1. These are slightly smaller, by a factor of 1.5–2, compared to our simulation. For the higher $\Sigma_{\rm gas}$ cases, however, the discrepancies are larger. For Σ55-KS and Σ150-KS, our $\eta_{\rm m}$ are 0.9 ± 0.3 and 0.2 ± 0.05, whereas theirs are 0.2 and 0.03, smaller by a factor of 4–7 than our values; for $\eta_{\rm E}$, our values are around 0.2 for both cases, whereas theirs are around 0.05, smaller by a factor of 4. In a follow-up paper, Creasey et al. (2015) measure the metal loading efficiency of the outflows for some runs in Creasey et al. (2013). Our model parameters only overlap with theirs for the solar neighborhood, in which we have $\eta_{\rm met} = 0.65 \pm 0.2$ and they have a smaller ≈0.2. Note also that we both assume a KS relation to relate $\Sigma_{\rm gas}$ and $\dot{\Sigma}_{\rm SFR}$, but we convert the SFR to SN rate by assuming $m_0 = 150\,M_\odot$ (definition of m_0 in Section 2.3), whereas they have $m_0 = 100\,M_\odot$. This means the difference is even larger by a factor of 1.5. We attribute the discrepancies mainly to their adoption of a cooling cut-off at 10^4 K. As a result, the neutral gas layer in their runs is thicker, and most SNe lose their energy there, thus the loading factors are smaller (see Section 4.2 for detailed discussions).

4.6. A Brief Summary and Some Missing Physics

Under the impact of many SN blast waves, the ISM becomes multiphase. The cooler, denser phase settles down near the midplane, whereas the hotter phases escape and form outflows. There are two regimes of the media: (i) a warm/cool-dominated ISM where, if an SN explodes within, it would lose most energy by radiative cooling, and (ii) a hot-dominated ISM, where SN shock waves would propagate much faster and further, while the cooling is inefficient (Cowie et al. 1981; Li et al. 2015). The fraction of SNe that explode in a

hot-dominated ISM, $f_{\rm SN,h}$, is key in determining the efficiency of the loading efficiency of energy and metals. A stronger external g-field or a weaker PEH leads to a smaller $h_{\rm gas}$, leaving more SNe exploding in the low-density medium, thus a more powerful loading of energy and metals; a larger $h_{\rm SN,cc}$ has a similar effect. Simply enhancing the SN rate, without changing $h_{\rm SN,cc}$ or $h_{\rm gas}$, yields unchanged energy and metal loading. The mass loading factor, on the other hand, has a more complex dependence on $f_{\rm SN,h}$: a $f_{\rm SN,h}$ that is either too small or too large would result in a small mass loading factor.

We briefly discuss the possible impact of the physics that we do not include in this work.

Under-resolved SNe. The resolution and $R_{\rm inj}$ for each run are fixed, and are chosen based on $R_{\rm cool}$ for the initial $\rho_{\rm mid}$. Later, when the ISM becomes multiphase, SNe exploding in the tenuous/hot phase continue to be well resolved. For all fiducial runs, the hot gas volume fraction at the midplane is 60%–80%. Since SNe are randomly located, a similar fraction of SNe would explode in the hot phase. The remaining SNe which explode in the denser phase are likely under-resolved, but we argue that these SNe are unimportant in driving large-scale outflows. Taking Σ10-KS for example, the cold phase has a density of about 10 cm^{-3}, corresponding to a $R_{\rm cool}\sim 7$ pc. So even when the evolution of the SNR is resolved spatially and temporally, it will lose the majority of its energy at $R_{\rm cool}$. This means that these SNe only have a very localized impact, and contribute little to large-scale outflows.

Magnetic fields. In the solar neighborhood, the magnetic pressure is overall similar to the thermal pressure of gas, and even larger for dense phases (Heiles & Crutcher 2005). This extra pressure, if included, would be likely to enhance $h_{\rm gas}$, and also make SN bubbles smaller (Slavin & Cox 1993). The net effect on the loading factors would be similar to having a stronger PEH—the energy and metal loadings would be smaller, while the change of the mass loading is not certain. The magnetic field on the dynamics of the diffuse ISM is rather mild for the solar neighborhood (de Avillez & Breitschwerdt 2005; Hill et al. 2012; Walch et al. 2015), except possibly for providing support for the vertical distribution of the gas (Cox 2005). Magnetic fields alone are unlikely to play an active role in driving the outflows.

Self-gravity. We did not incorporate self-gravity in our simulations. For the solar neighborhood, only about 1% of the volume is in a self-gravitating state (Draine 2011). For larger gas surface density cases, however, self-gravity is probably more important. Including self-gravity would make the cold phase smaller in volume, thus may facilitate feedback for those SNe that explode in the inter-cloud space (e.g., Girichidis et al. 2016b; Kim & Ostriker 2016). But we note that (i) the external gravitational field in our simulations does include that from the gas, so the effect of self-gravity is not fully missed, at least in the vertical direction. (ii) As mentioned in Section 3.1, essentially in all runs, the volume fraction of hot gas at the midplane is 60%–80%, thus we believe shrinking the volume fraction of cold gas by some percentage would not lead to a qualitative change in the loading factors of outflows. (iii) Self-gravity should be included with caution; that is, one should also resolve the counterbalancing force—feedback acting below the Jeans scale of the dense clumps, which is challenging given the resolution of the current ISM simulations; otherwise, most gas would collapse into a few small clumps, which is also not realistic.

Cosmic rays (CRs). SNe are considered to be the main acceleration sites for CRs. Around 5%–15% of SNe energy may go into CRs (Hillas 2005). Recent simulations show CRs are promising candidates to drive galactic scale outflows, with a mass loading around 0.5 (Uhlig et al. 2012; Booth et al. 2013; Hanasz et al. 2013; Salem & Bryan 2014). Recent high-resolution, local simulations indicate that for the solar neighborhood, both CRs and SN thermal feedback can drive an outflow with mass loading around unity (Girichidis et al. 2016a; Simpson et al. 2016). CR-driven outflows are cooler, slower, and smoother than thermally driven ones. Peters et al. (2015) point out that compared to thermal feedback, CR-driven outflows give too little hot gas to match the soft X-ray background. Many questions remain open regarding how CRs propagate in, and interact with, a multiphase ISM. Further work is needed to determine whether thermal feedback or CRs are the dominant force launching outflows.

Radiation pressure. Radiation pressure can propel gas out if it is optically thick, especially for infrared light. The photon energy from the stars can then be effectively utilized to drive outflows (Murray et al. 2005; Hopkins et al. 2012). This can be the case for the extremely dense and dusty SF regions, such as in the ultra-luminous infrared galaxies (ULIRGs). We do not actually explore those extreme cases (Figure 1). For the $\Sigma_{\rm gas}$ adopted in our models, the optical depth for the infrared is much less than unity, therefore the radiation pressure is not important.

We also do not include preprocessing of the ISM by other stellar feedbacks, such as stellar winds, ionizing photons, etc. In general these feedbacks alone do not contribute directly to launching outflows (unless the radiation is highly trapped), but they may make the ISM inhomogeneous. Therefore it is possible for SNe to explode in a less dense environment, thus facilitating SN feedback to some extent (e.g., Gatto et al. 2016; Peters et al. 2017).

5. Discussion

5.1. Hot Outflows and Hot CGM

Hot, X-ray-emitting coronae have been observed around the MW (Snowden et al. 1998) and other star-forming disk galaxies, up to a few tens of kpc away from the galaxy (Strickland et al. 2004; Tüllmann et al. 2006; Anderson & Bregman 2011; Dai et al. 2012). Hot gas around the MW is also detected through O VII and O VIII absorption lines (Fang et al. 2006; Bregman & Lloyd-Davies 2007; Gupta et al. 2012). The COS–Halos survey finds the warm-hot metal-enriched gas out to $\gtrsim$100 kpc for MW-like galaxies, as traced by the O VI absorption lines (Tumlinson et al. 2011). Our simulations indicate that the hot phase in the outflows has the largest v_z and $v_{\widetilde{B}}$, and can potentially travel distances comparable to the size of DM halos. Hot outflows carry 10%–50% of energy and 30%–50% of metals produced by SNe (Section 3.3). Thus, the hot, metal-enriched CGM may at least be partly due to these SNe-driven outflows. Those outflows should have an important dynamic impact on the CGM (Hopkins et al. 2012).

Recently, Faerman et al. (2016) create a two-phase phenomenological model of the halo gas for MW-like galaxies, which simultaneously fits the absorption features of O VI, O VII, and O VIII. The two phases in their model have volume-weighted medium temperatures of 3×10^5 K and 1.8×10^6 K. Nearly 90% of the mass is in the hotter phase. The total masses of the two phases are comparable to that of the baryons in the

DM halo but not in the galaxy. Our hot phase in Σ10-KS and Σ10-KS-4g has a temperature comparable to that in their model. We note, though, that the cooling luminosity of the CGM in their model is about twice the SNe heating rate from the MW, and given that $\eta_{\rm E} \approx 0.45$ for the MW-average, the total discrepancy is about a factor of 4.

5.2. Cool Outflows

Warm/cool outflows are observed through interstellar absorption lines, which have velocities of about several hundred $\rm km\,s^{-1}$ (Steidel et al. 1996; Shapley et al. 2003; Martin 2005; Weiner et al. 2009; Heckman et al. 2015). Mass loading factors around a few are frequently reported. In our simulations, the cool phase in general does not have such high velocities, and the mass loading is usually smaller than unity, especially for high $\Sigma_{\rm gas}$. We here discuss the possible reasons for this apparent discrepancy.

We first note that observations usually focus on the star-bursting regime, such as (U)LIRGs and Lyman break galaxies, which we do not cover in our simulations (Figure 1). As mentioned before, radiation pressure may account for the potential high mass loading in those extreme environments, provided that the infrared light can be trapped by dust. Note that those bursting SF systems are very rare; even at higher redshifts where they are more common, they only account for $\lesssim$10% of cosmic SF density (Rodighiero et al. 2011).

Second, the observed mass loading factors have large uncertainties, due to the unconstrained metallicity, ionization fraction, geometry, etc. This can lead to an error bar as large as the mass loading factor itself. Recent work by Chisholm et al. (2016), which claims a better constraints on the above quantities, suggests a small $\eta_{\rm m} \approx 0.1$. This is, in fact, not inconsistent with our value for the highest $\Sigma_{\rm gas}$.

On the simulation side, we note that even though we adopt high enough resolution to make sure the Sedov–Taylor phase of SNRs is well-resolved, the interaction between different gas phases may still not be sufficiently resolved, once the ISM becomes multiphase. To what extent this may affect the mass loading is not clear.

Another apparent discrepancy is that we find that the cooler phases dominate less of the outflow mass flux for higher $\dot{\Sigma}_{\rm SFR}$. It is possible, however, that some cool clouds may form on the way due to thermal instability (Field 1965; Thompson et al. 2016), which we do not capture because of the relatively small box size. But again, how much cool mass would form under this mechanism is not clear.

Overall, there remains much uncertainty about the observational interpretation and theoretical modeling of cool outflows.

5.3. Implications for Cosmological Simulations

Stellar feedback is one of the key ingredients for galaxy formation in cosmological simulations and semi-analytic models (Somerville & Davé 2015). The general consensus is that strong feedback/outflows are needed to reproduce various observed scaling relations of galaxies (Springel & Hernquist 2003; Stinson et al. 2006; Hopkins et al. 2012; Hummels & Bryan 2012). Due to the limited resolution in cosmological simulations, however, a multiphase ISM and individual SNRs cannot be resolved. Ad hoc models are widely used in the field, with free parameters fine-tuned to match observations. Different groups adopt very different recipes, usually invoking shutting off cooling or hydrodynamics. To evaluate the real impact of feedback, however, a physically grounded model is necessary. While formulating such a model is beyond the scope of this paper, we compare the loading factors found in our work to current cosmological simulations, and briefly discuss the implications.

In cosmological simulations, a significant fraction of SNe energy is used to generate outflows, roughly 30%–50% (e.g., Oppenheimer & Davé 2008). Our $\eta_{\rm E}$ varies from 15% to 50%, broadly consistent with that fraction. To match the observed mass–metallicity relation of galaxies, a significant fraction of metals has to be driven out of the galaxies. Our $\eta_{\rm met}$ is about 40%–80%, in general agreement with what observations require and cosmological simulations adopt. The main difference is the mass loading of the outflows or, in other words, the amount of mass that those energy and metals couple to. Our $\eta_{\rm m}$ is in general smaller than what is adopted in cosmological simulations, by roughly an order of magnitude. A smaller mass loading is not surprising for the simulations where the multiphase ISM is resolved: SN blast waves tend to vent through the least-obstructed channel, thus preferentially heating and accelerating the tenuous phase (Cowie et al. 1981; Li et al. 2015). Cosmological simulations cannot resolve the multiphase ISM/outflows generally. Mixing the fast/tenuous and the slow/dense phase due to insufficient resolution would result in slower, cooler, and mass-loaded outflows. Therefore current cosmological simulations may not accurately predict the impacts of galactic outflows on the CGM and galaxy formation. From our simulations, hot outflows, though not carrying a great amount of mass, may be able to suppress the inflows given their vigor (Section 3.2), therefore restricting galaxy masses. The implications of tenuous yet vigorous hot outflows to galaxy formation and the CGM are not clear (although see recent attempts by Davé et al. 2016 & Fielding et al. 2017).

6. Summary

In this paper, we use high-resolution simulations to study the multiphase outflows driven by SNe from stratified media. We cover a wide range of $\Sigma_{\rm gas}$: 1–150 $M_\odot\,{\rm pc}^{-2}$. We quantify the multiphase outflows by measuring the loading factors of energy, mass, and metals. The fiducial runs assume $\Sigma_{\rm gas}$ scales with $\dot{\Sigma}_{\rm SFR}$ as in the KS relation (Figure 1). We study the effects of various physics on the loading factors: SN scale height $h_{\rm SN,cc}$, PEH, external gravitational field, and enhanced SN rate. Here are our main conclusions.

1. The ISM quickly becomes multiphase under the impact of multiple SNe. The cold phase settles down near the midplane, whereas hotter phases preferentially escape and form outflows.
2. For the solar neighborhood case, the gas pressure, volume fraction of hot gas, and mean densities of different gas phases agree well with the observations.
3. The mass loading factor $\eta_{\rm m}$ decreases monotonically with increasing $\Sigma_{\rm gas}$ as $\eta_{\rm m} \propto \Sigma_{\rm gas}^{-0.6}$ (Equation (8)). The outflowing flux is about 0.1–10 of $\dot{\Sigma}_{\rm SFR}$. The energy and metal loading factors do not show significant variance with $\Sigma_{\rm gas}$. Roughly 10%–50% of the energy and 40%–80% of the metals produced by SNe are carried away by the outflows (Figure 10).

4. More of the outflow volume is occupied by hot gas ($T > 3 \times 10^5$ K) for larger $\Sigma_{\rm gas}$. The hot phase contributes to $\gtrsim 1/3$ of the mass loading, >0.8 of the energy loading, and 0.5–0.9 of the metal loading (Figure 10). It has significantly larger v_z and $v_{\widetilde{\mathcal{B}}}$ (see Section 3.2 for a definition) than the cooler phases. Hot outflows are very likely to have a broad impact on the CGM.
5. Increasing $h_{\rm SN}$ enhances the energy and metal loading, since more energy/metals are directly deposited into the low-density halo. The mass loading factor, on the other hand, does not show a monotonic dependence on $h_{\rm SN}$. The relative scale height of SNe and gas is a very important factor determining the loading efficiencies. Various physical processes affect the loading factors by changing $h_{\rm SN}$ and/or $h_{\rm gas}$.
6. A stronger PEH makes SN feedback less effective, since it keeps more gas in the warm phase, thus a larger scale height of the neutral gas layer. In the extreme case where the cooling curve has a lower cut-off at 10^4 K, the feedback is severely suppressed, with the loading factors smaller by a factor of $\gtrsim$10. (Figures 12 and 13).
7. A larger gravitational field, by lowering $h_{\rm SN,cc}$, may result in much stronger energy and metal loading (Figure 15).
8. If the SN rate is enhanced above the KS relation, the energy and metal fluxes roughly scale linearly with the SN rate, but the mass flux has a sub-linear dependence on the SN rate. Overall, once the ISM is hot-dominated, clustering SNe does not enhance the time-integrated properties of outflows.

We thank the referee for comments that helped to improve the clarity of the paper. We thank Thorsten Naab for very helpful comments on the manuscript, and Eve Ostriker for interesting discussions on the topic. Computations described in this work were performed using the publicly available Enzo code (http://enzo-project.org), which is the product of a collaborative effort of many independent scientists from numerous institutions around the world. Their commitment to open science has helped make this work possible. The visualization was partly done using the **yt** project (Turk et al. 2011). This work utilized the following computing resources: the Extreme Science and Engineering Discovery Environment (XSEDE) supported by National Science Foundation grant number ACI-1053575, the NASA HECC Pleiades Supercomputer (under accounts of s1670 and s1529), the Hecate cluster at Princeton University, and the Yeti cluster at Columbia University. The authors acknowledge financial support from NASA grant NNX15AB20G and NSF grants AST-1312888 and AST-1615955.

References

Anderson, M. E., & Bregman, J. N. 2011, ApJ, 737, 22
Bigiel, F., Leroy, A., Walter, F., et al. 2008, AJ, 136, 2846
Binney, J., & Tremaine, S. 2008, Galactic Dynamics (2nd ed.; Princeton, NJ: Princeton Univ. Press)
Bolatto, A. D., Warren, S. R., Leroy, A. K., et al. 2013, Natur, 499, 450
Booth, C. M., Agertz, O., Kravtsov, A. V., & Gnedin, N. Y. 2013, ApJL, 777, L16
Bregman, J. N., & Lloyd-Davies, E. J. 2007, ApJ, 669, 990
Bryan, G. L., Norman, M. L., O'Shea, B. W., et al. 2014, ApJS, 211, 19
Bustard, C., Zweibel, E. G., & D'Onghia, E. 2016, ApJ, 819, 29
Chen, Y.-M., Tremonti, C. A., Heckman, T. M., et al. 2010, AJ, 140, 445
Chisholm, J., Tremonti, C. A., Leitherer, C., & Chen, Y. 2016, arXiv:1605.05769
Colella, P., & Woodward, P. R. 1984, JCoPh, 54, 174
Cowie, L. L., McKee, C. F., & Ostriker, J. P. 1981, ApJ, 247, 908
Cox, D. P. 2005, ARA&A, 43, 337
Cox, D. P., & Smith, B. W. 1974, ApJL, 189, L105
Creasey, P., Scannapieco, C., Nuza, S. E., et al. 2015, ApJL, 800, L4
Creasey, P., Theuns, T., & Bower, R. G. 2013, MNRAS, 429, 1922
Dai, X., Anderson, M. E., Bregman, J. N., & Miller, J. M. 2012, ApJ, 755, 107
Davé, R., Thompson, R., & Hopkins, P. F. 2016, MNRAS, 462, 3265
de Avillez, M. A. 2000, MNRAS, 315, 479
de Avillez, M. A., & Breitschwerdt, D. 2005, A&A, 436, 585
Draine, B. T. 1978, ApJS, 36, 595
Draine, B. T. 2011, Physics of the Interstellar and Intergalactic Medium (Princeton NJ: Princeton Univ. Press)
Efstathiou, G. 2000, MNRAS, 317, 697
Erb, D. K., Shapley, A. E., Pettini, M., et al. 2006, ApJ, 644, 813
Faerman, Y., Sternberg, A., & McKee, C. F. 2016, arXiv:1602.00689
Fang, T., Mckee, C. F., Canizares, C. R., & Wolfire, M. 2006, ApJ, 644, 174
Field, G. B. 1965, ApJ, 142, 531
Fielding, D., Quataert, E., McCourt, M., & Thompson, T. A. 2017, MNRAS, 466, 3810
Freeman, K. C. 1987, ARA&A, 25, 603
Fujita, A., Mac Low, M.-M., Ferrara, A., & Meiksin, A. 2004, ApJ, 613, 159
Gatto, A., Walch, S., Low, M.-M. M., et al. 2015, MNRAS, 449, 1057
Gatto, A., Walch, S., Naab, T., et al. 2016, arXiv:1606.05346
Genel, S., Fall, S. M., Hernquist, L., et al. 2015, ApJL, 804, L40
Gent, F. A., Shukurov, A., Fletcher, A., Sarson, G. R., & Mantere, M. J. 2013, MNRAS, 432, 1396
Genzel, R., Newman, S., Jones, T., et al. 2011, ApJ, 733, 101
Gilmore, G., & Reid, N. 1983, MNRAS, 202, 1025
Girichidis, P., Naab, T., Walch, S., et al. 2016a, ApJL, 816, L19
Girichidis, P., Walch, S., Naab, T., et al. 2016b, MNRAS, 456, 3432
Governato, F., Willman, B., Mayer, L., et al. 2007, MNRAS, 374, 1479
Gupta, A., Mathur, S., Krongold, Y., Nicastro, F., & Galeazzi, M. 2012, ApJL, 756, L8
Hanasz, M., Lesch, H., Naab, T., et al. 2013, ApJL, 777, L38
Heckman, T. M., Alexandroff, R. M., Borthakur, S., Overzier, R., & Leitherer, C. 2015, ApJ, 809, 147
Heckman, T. M., Sembach, K. R., Meurer, G. R., et al. 2001, ApJ, 554, 1021
Heiderman, A., Evans, N. J., II, Allen, L. E., Huard, T., & Heyer, M. 2010, ApJ, 723, 1019
Heiles, C., & Crutcher, R. 2005, in Cosmic Magnetic Fields, ed. R. Wielebinski & R. Beck (Berlin: Springer), 137
Heiles, C., & Troland, T. H. 2003, ApJ, 586, 1067
Hennebelle, P., & Iffrig, O. 2014, A&A, 570, A81
Hill, A. S., Joung, M. R., Mac Low, M.-M., et al. 2012, ApJ, 750, 104
Hillas, A. M. 2005, JPhG, 31, R95
Hopkins, P. F., Quataert, E., & Murray, N. 2012, MNRAS, 421, 3522
Hummels, C. B., & Bryan, G. L. 2012, ApJ, 749, 140
Joung, M. K. R., & Mac Low, M.-M. 2006, ApJ, 653, 1266
Joung, M. R., Mac Low, M.-M., & Bryan, G. L. 2009, ApJ, 704, 137
Kim, C.-G., & Ostriker, E. C. 2015, ApJ, 802, 99
Kim, C.-G., & Ostriker, E. C. 2016, arXiv:1612.03918
Kuijken, K., & Gilmore, G. 1989, MNRAS, 239, 605
Li, M., Ostriker, J. P., Cen, R., Bryan, G. L., & Naab, T. 2015, ApJ, 814, 4
Mac Low, M.-M., & Ferrara, A. 1998, in IAU Colloq. 166, The Local Bubble and Beyond, ed. D. Breitschwerdt, M. J. Freyberg, & J. Truemper (Berlin: Springer), 559
Mac Low, M.-M., & Ferrara, A. 1999, ApJ, 513, 142
Martin, C. L. 2005, ApJ, 621, 227
McKee, C. F., & Ostriker, J. P. 1977, ApJ, 218, 148
Mitchell, R. J., Culhane, J. L., Davison, P. J. N., & Ives, J. C. 1976, MNRAS, 175, 29P
Murray, N., Quataert, E., & Thompson, T. A. 2005, ApJ, 618, 569
Naab, T., & Ostriker, J. P. 2016, arXiv:1612.06891
Narayan, R., & Ostriker, J. P. 1990, ApJ, 352, 222
Navarro, J. F., Frenk, C. S., & White, S. D. M. 1997, ApJ, 490, 493
Oppenheimer, B. D., & Davé, R. 2006, MNRAS, 373, 1265
Oppenheimer, B. D., & Davé, R. 2008, MNRAS, 387, 577
Peters, T., Girichidis, P., Gatto, A., et al. 2015, ApJL, 813, L27
Peters, T., Naab, T., Walch, S., et al. 2017, MNRAS, 466, 3293
Rodighiero, G., Daddi, E., Baronchelli, I., et al. 2011, ApJL, 739, L40
Rosen, A., & Bregman, J. N. 1995, ApJ, 440, 634
Rupke, D. S., Veilleux, S., & Sanders, D. B. 2002, ApJ, 570, 588

Salem, M., & Bryan, G. L. 2014, MNRAS, 437, 3312
Scannapieco, C., Tissera, P. B., White, S. D. M., & Springel, V. 2008, MNRAS, 389, 1137
Schaye, J., Aguirre, A., Kim, T.-S., et al. 2003, ApJ, 596, 768
Shapley, A. E., Steidel, C. C., Pettini, M., & Adelberger, K. L. 2003, ApJ, 588, 65
Simpson, C. M., Bryan, G. L., Hummels, C., & Ostriker, J. P. 2014, arXiv:1410.3822
Simpson, C. M., Pakmor, R., Marinacci, F., et al. 2016, arXiv:1606.02324
Slavin, J. D., & Cox, D. P. 1993, ApJ, 417, 187
Snowden, S. L., Egger, R., Finkbeiner, D. P., Freyberg, M. J., & Plucinsky, P. P. 1998, ApJ, 493, 715
Somerville, R. S., & Davé, R. 2015, ARA&A, 53, 51
Songaila, A., & Cowie, L. L. 1996, AJ, 112, 335
Springel, V., & Hernquist, L. 2003, MNRAS, 339, 312
Steidel, C. C., Giavalisco, M., Pettini, M., Dickinson, M., & Adelberger, K. L. 1996, ApJL, 462, L17
Stinson, G., Seth, A., Katz, N., et al. 2006, MNRAS, 373, 1074
Strickland, D. K., Heckman, T. M., Colbert, E. J. M., Hoopes, C. G., & Weaver, K. A. 2004, ApJS, 151, 193
Thompson, T. A., Quataert, E., Zhang, D., & Weinberg, D. H. 2016, MNRAS, 455, 1830
Tremonti, C. A., Heckman, T. M., Kauffmann, G., et al. 2004, ApJ, 613, 898
Tüllmann, R., Pietsch, W., Rossa, J., Breitschwerdt, D., & Dettmar, R.-J. 2006, A&A, 448, 43
Tumlinson, J., Thom, C., Werk, J. K., et al. 2011, Sci, 334, 948
Turk, M. J., Smith, B. D., Oishi, J. S., et al. 2011, ApJS, 192, 9
Turner, M. L., Schaye, J., Steidel, C. C., Rudie, G. C., & Strom, A. L. 2015, MNRAS, 450, 2067
Uhlig, M., Pfrommer, C., Sharma, M., et al. 2012, MNRAS, 423, 2374
Veilleux, S., Cecil, G., & Bland-Hawthorn, J. 2005, ARA&A, 43, 769
Walch, S., Girichidis, P., Naab, T., et al. 2015, MNRAS, 454, 238
Walter, F., Weiss, A., & Scoville, N. 2002, ApJL, 580, L21
Wang, Q. D., Li, J., Jiang, X., et al. 2016, MNRAS, 457, 1385
Weiner, B. J., Coil, A. L., Prochaska, J. X., et al. 2009, ApJ, 692, 187
Wolfire, M. G., Hollenbach, D., McKee, C. F., Tielens, A. G. G. M., & Bakes, E. L. O. 1995, ApJ, 443, 152
Wolfire, M. G., McKee, C. F., Hollenbach, D., & Tielens, A. G. G. M. 2003, ApJ, 587, 278
Zhang, D., Thompson, T. A., Murray, N., & Quataert, E. 2014, ApJ, 784, 93